Nano Research

Open Access

Research Article

Tandem design of conductivity-enhanced electrochromic electrode for multi-spectra modulation smart window

Meng-Han Zhu[1,2,§], Si-Zhe Sheng[1,2,§], Xue-Feng Huang[1,2], Chen Chen[1,2], Zong-Ying Huang[1,2], Fu-Xing Zhao[1,2], Jin-Long Wang[1,2] ✉, and Shu-Hong Yu[2,3] ✉

[1] *State Key Laboratory of Quantum Functional Materials, Department of Materials Science and Engineering, Southern University of Science and Technology, Shenzhen 518055, China*

[2] *Shenzhen Key Laboratory of Sustainable Biomimetic Materials, Guangdong Provincial Key Laboratory of Sustainable Biomimetic Materials and Green Energy, Institute of Major Scientific Facilities for New Materials, Guangming Advanced Research Institute, Department of Chemistry Southern University of Science and Technology, Shenzhen 518055, China*

[3] *New Cornerstone Science Laboratory, Division of Nanomaterials & Chemistry Hefei National Research Center for Physical Sciences at the Microscale, Department of Chemistry, Institute of Biomimetic Materials & Chemistry, Anhui Engineering Laboratory of Biomimetic Materials University of Science and Technology of China, Hefei 230026, China*

§ *Meng-Han Zhu and Si-Zhe Sheng contributed equally to this work.*

Cite this article: *Nano Research*, **2026**, *19*, 94908696. https://doi.org/10.26599/NR.2026.94908696

ABSTRACT: Overcoming the constraint of single-color display by integrating diverse electrochromic materials within a single electrode can facilitate the practical utilization of electrochromic devices. However, the mutual interference between different electrochromic materials during operation is always inevitable. In this study, a multimode electrochromic electrode is demonstrated by assembling the porous anodic (NiO nanosheets) and cathodic ($W_{18}O_{49}$ nanowire networks) electrochromic materials in a tandem structure with a conductive ITO interlayer inserted in between on the same electrode. The open framework ensures sufficient electrolyte penetration for the anodic and cathodic materials to operate independently, and the incorporation of the ITO interlayer lowers the effective work function of the electrochromic electrode and facilitates electron transport, leading to a 14.46% and 53.4% reduction in coloring and bleaching time of the outer-layer $W_{18}O_{49}$ nanowire network from 10.1/7.06 to 8.64/3.29 s, as well as a 31.7% enhancement in coloration efficiency from 54.02 to 71.15 cm²/C. Thus, the electrochromic electrode employing a tandem structural design effectively achieves dynamic transparent, brown, and blue optical states under different biases, while achieving modulation of the visible and near-infrared spectral bands, offering a viable pathway for high-performance multimode smart windows and multicolor displays.

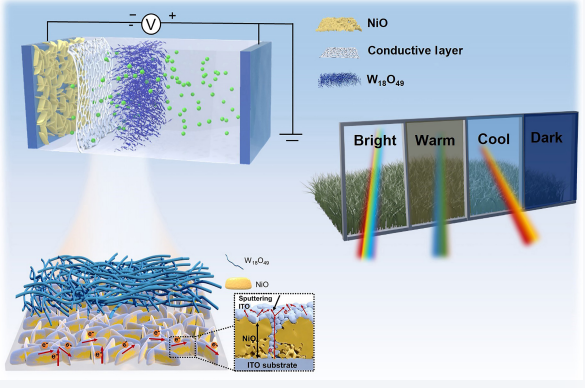

KEYWORDS: assembly, nanowire, electrochromism, multi-spectra modulation, smart window

1 Introduction

Electrochromism (EC) refers to the reversible change in the optical properties (such as absorptance, transmittance, or reflectance) of certain materials induced by electrochemically driven redox reactions, which are accompanied by the insertion/extraction of ions and electrons under an applied electrical potential [1–3]. The inorganic electrochromic materials (EM) with high stability have played a critical role in developing the next-generation smart window technology in the energy efficiency buildings [4, 5]. Among various inorganic electrochromic materials, oxygen-deficient tungsten oxide (WO_{3-x}) has attracted particular attention due to its high transmittance contrast and strong plasmonic absorption in the near-infrared region since its initial study by Deb in 1969 [6]. However, its practical application is still hindered by challenges such as simple color adjustment and the inability to perform multiband selective modulation. To address color monotonicity, extensive research has focused on integrating WO_{3-x} with optical

Received: January 24, 2026; **Revised:** March 30, 2026
Accepted: March 31, 2026

✉Address correspondence to Jin-Long Wang, wangjl6@sustech.edu.cn; Shu-Hong Yu, yush@sustech.edu.cn

resonators, designing plasmonic or Fabry–Perot structures to improve the color tunability of WO_{3-x}-based electrochromic devices [7–9]. Alternatively, the transmittance and color of the device can be easily controlled by co-assembling WO_{3-x} and V_2O_5 [10]. Although the structures mentioned above can produce vibrant colors, they result in a lack of colorless transparency of devices. The colorless intermediate state is a fundamental aspect of the extensive applicability of electrochromic devices in various fields, including energy conservation, temperature regulation, camouflage, and anti-counterfeiting technology [11–14].

In addition, multi-component composite structures with functional integration are demonstrated as another promising approach to enable device transparency and multiband regulation [15–18]. For instance, WO_{3-x} and NiO, which exhibit disparate electrochromic characteristics, are deposited on discrete electrodes to attain multicolor display in a single electrochromic device. However, the composite structure is susceptible to impairing the electrochromic performance, predominantly due to the impeded electron and ion conduction resulting from inadequate contact between the electrochromic layer and the conductive or electrolyte layer [19, 20]. In recent years, it has been reported that increasing the contact between the electrochromic materials and conductive materials can promote charge transfer, thereby enhancing the electrochromic performance of the device, including response time, coloring efficiency, and more performance parameters [21–23]. Recently, constructing highly conductive networks or composite structures has been proven to be a highly effective strategy to overcome the sluggish kinetics of conventional electrochromic materials. For instance, Gao et al. integrated WO_3 with ITO nanoparticles or silver nanowires (Ag NWs), where the introduction of these conductive networks significantly enhances electron transport and ion diffusion, resulting in improved response kinetics and coloration efficiency [24, 25]. Notably, this effective strategy for performance enhancement mainly focuses on the single electrochromic material system. It is desirable to design the conductive layer between multi-component materials in composite structures to realize high-performance, multiband spectral regulated electrochromic devices.

In this work, an integrated anodic/cathodic electrochromic electrode with a NiO/ITO/$W_{18}O_{49}$ (NIW) tandem architecture is constructed via a layer-by-layer assembly strategy, enabling transparent, brown, and blue optical states under different applied potentials. The pre-synthesized porous NiO nanosheets and the spray-coated $W_{18}O_{49}$ nanowires ensure the open hierarchical framework of the tandem structure that facilitates efficient electrolyte infiltration throughout the electrode. Importantly, the introduced ITO interlayer serves as an effective conductive bridge, promoting electron transport during the electrochromic processes of both NiO and $W_{18}O_{49}$ and thereby significantly accelerating the device response. This architecture decouples the electrochromic responses of anodic and cathodic materials, enabling interference-free color expression and wavelength-selective modulation. As a result, this simple architecture features selective spectral modulation characteristics for visible light of 400–800 nm (VIS) and near-infrared spectrum of 800–1600 nm (NIR), making it a promising design for optical modulation devices.

2 Experimental

2.1 Materials

In_2O_3:Sn (ITO) coating glasses with a resistance of 7–10 Ω/sq were purchased from TCXKBIO. Co., Ltd. Nickel nitrate ($Ni(NO_3)_2·6H_2O$) was purchased from Shanghai Aladdin Biochemical Technology Co., Ltd. Tungsten hexachloride (WCl_6) was purchased from Heowns Biochem Technologies. Lithium perchlorate ($LiClO_4$) was purchased from Shanghai Aladdin Biochemical Technology Co., Ltd. Propylene carbonate was purchased from Shanghai Maclin Biochemical Technology Co., LTD. Other reagents were used without further purification.

2.2 Synthesis of NiO film

The NiO nanosheets were synthesized by electrodeposition on ITO glass. ITO glass (1 cm × 4 cm) with a sheet resistance of about 7–10 Ω/sq was immersed into 0.01 M nickel nitrate ($Ni(NO_3)_2·6H_2O$) aqueous solution for the electrodeposition experiment. Prior to electrodeposition, ITO glass was continuously cleaned in acetone, ethanol, and deionized aqueous solutions for 30 min. The standard three-electrode system was used for electrochemical deposition. ITO conductive glass was used as the working electrode (WE); platinum wire (Pt, purity 99.99%) was the counter electrode (CE); Ag/AgCl was the reference electrode (RE). Electrodeposition was carried out at a low current density of −0.05 mA/cm^2 for 1200 s. After electrodeposition, the film was cleaned and dried, and then annealed at 300 °C for 1 h to obtain the NiO film with 170 nm thickness.

2.3 Synthesis of $W_{18}O_{49}$ nanowires

The $W_{18}O_{49}$ nanowires were synthesized by the solvothermal method. 0.06 g WCl_6 was added to 80 mL of ethanol to form a uniform solution under intense agitation. Then, the solution was transferred to a 100 mL Teflon-liner and heated in a stainless-steel autoclave to 180 °C for 24 h. After the reaction, the products were centrifuged and redispersed in ethanol with a concentration of 1.5 mg/mL for further application.

2.4 Deposition of ITO thin film

A thin film of ITO was deposited by reactive DC magnetron sputtering. The ITO target was 10 cm away from the substrate (NiO-ITO glass). The power was set at 130 W, and the pressure was maintained at 0.5 Pa during sputtering. When the vacuum in the chamber reached 6 × 10^{-5} Pa, the samples were pre-sputtered for 5 min in argon. During sputtering, the substrate was rotated to ensure a uniform coating. The thickness of the film prepared in this paper was about 50/100/150 nm, which can change with the change of deposition time.

2.5 Fabrication of NW and NIW films

The NiO/$W_{18}O_{49}$ (NW) and NIW films were prepared by spraying different amounts of $W_{18}O_{49}$ nanowire solution onto the NiO-ITO glass and ITO-NiO-ITO glass that were fixed on the 80 °C hot plate using an airbrush with a diameter of 0.3 μm. The nozzle position of the control gun was 4 cm away from the substrate. The prepared composite film was annealed at 120 °C for 10 min to obtain the EC film.

2.6 Fabrication of the NW and NIW based electrochromic device

The electrochromic device was assembled using two pieces of ITO glass (4 cm × 4 cm) with NiO/ITO/$W_{18}O_{49}$/LiTFSI-HPMC gel electrolyte/NiO. The ultraviolte (UV)-curing adhesive was used to seal the EC device. Prior to undergoing any testing, the assembled

EC devices were allowed to dry thoroughly in the ambient air for a full day, ensuring optimal performance and stability.

The electrochromic device featuring a butterfly pattern was assembled using two pieces of ITO glass. The conductive layer in the middle of the ITO glass was removed by chemically etching with hydrochloric acid and zinc particles. The subsequent steps followed the same procedure as previously described for device assembly.

2.7 Characterization

The surface morphology was studied by a cold-field high-resolution scanning electron microscope (SEM, Hitachi SU8230) at an accelerating potential of 5 kV. Transmission electron microscopy (TEM) images were taken using a Talos F200X G2 TEM operating at an accelerating potential of 200 kV. The crystalline shapes of NiO and $W_{18}O_{49}$ were analyzed by X-ray diffraction (XRD, Smartlab 3KW). Fine scanning of X-ray photoelectron spectroscopy (XPS) was carried out on a Thermo Fisher Scientific ESCALAB Xi+ with 30 eV pass energy and 0.1 eV step size. Ultraviolet photoelectron spectroscopy (UPS) spectra were measured using a non-monochromatic He I α photon source ($h\nu$ = 21.22 eV, Au is taken for calibration). The ultraviolet–visible–near infrared (UV–VIS–NIR) spectra were recorded on a UV-3600i Plus (Shimadzu Corporation) and tested at ambient temperature using an integrating sphere (ISR-1503) transmission mode. Atomic force microscopy (AFM) and conductive atomic force microscopy (C-AFM) (Cypher S, Oxford Instruments) were used to characterize the current and surface morphology of the obtained NiO and NiO/ITO samples. Infrared images over time were recorded by a Ti480 Pro thermal imager (Fluke), and temperature over time was recorded by a TA612C (TASI) thermocouple. The electrochemical tests were carried out on the electrochemical workstation (CHI 760E) on a three-electrode system, using the NW or NIW film as the working electrode, the Pt foil as the counter electrode and the Ag/AgCl as the reference electrode. The "Electrochemistry" module in COMSOL Multiphysics was adopted to simulate the distributions of Li^+ concentration gradient on NW and NIW electrodes. The ionic migration was calculated by "Nernst–Einstein" equation, while the diffusion coefficient and conductivity were determined by the specific electrolytes. The electrode reaction was based on the "Electrode Surface Species Flux Balance" equation. During the whole simulations, the upper boundary is set as the electrolyte and conductive substrate boundary with a current density of 5 mA/cm^2.

3 Results and discussion

3.1 Design of NIW electrode in tandem structure

The preparation process of the multimode electrochromic device is shown in Fig. 1(a). Owing to the tandem integration of anodic and cathodic electrochromic layers, the electrode reversibly switches among transparent, brown, and blue states under different applied potentials, enabling independent color expression as well as synergistic regulation of VIS and NIR for bright, warm, cool, and dark modes (Fig. 1(b)). A porous NiO nanosheet film was first electrodeposited *in situ* on conductive glass as the anodic electrochromic layer to separately modulate VIS. The elemental composition of the NiO film was determined by XPS

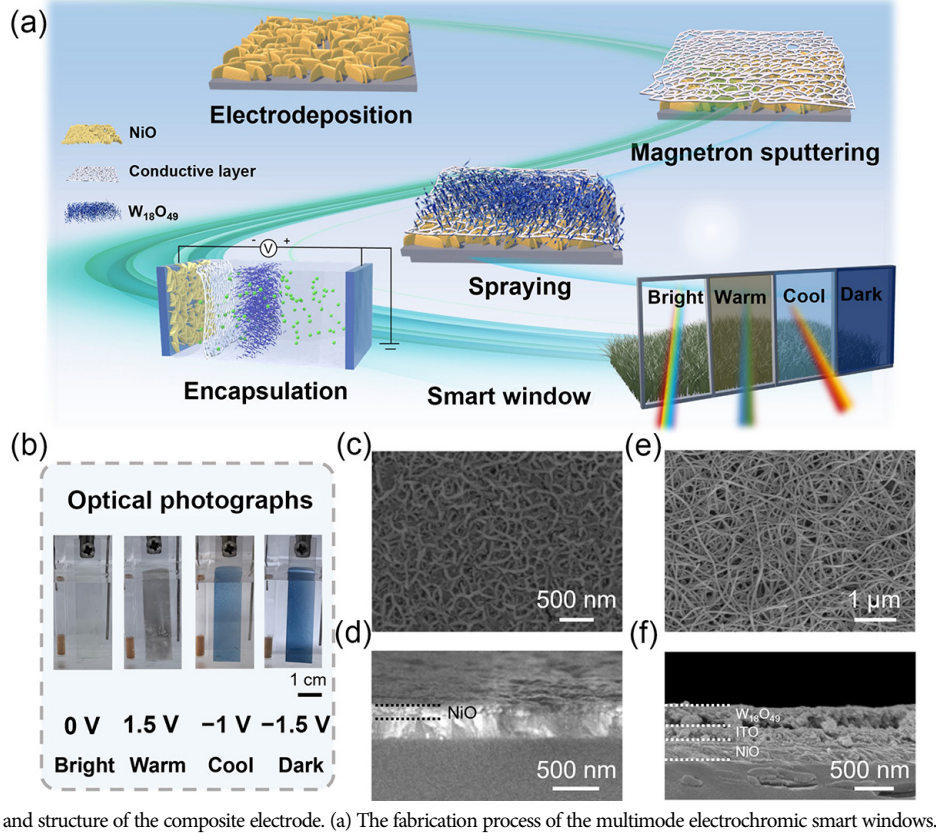

Figure 1 The fabrication and structure of the composite electrode. (a) The fabrication process of the multimode electrochromic smart windows. (b) Optical photographs of the composite electrode with four modes. (c) and (d) Surface and cross-sectional SEM images of the NiO electrode. (e) and (f) Surface and cross-sectional SEM images of the NIW electrode.

characterization (Fig. S1(a) in the Electronic Supplementary Material (ESM)). XRD pattern shows that the NiO film has a cubic rock salt structure ($Fm\bar{3}m$), with diffraction peaks at 37.3°, 43.3° and 62.9°, corresponding to (111), (200), and (220) plane indices and the other observed peaks belong to the ITO substrate layer (Fig. S2 in the ESM) [26, 27]. SEM and TEM images (Fig. 1(c) and Fig. S3(a) in the ESM) show that the NiO film consists of an interconnected nanosheet network with abundant open pores, and the cross-sectional SEM image (Fig. 1(d)) indicates a thickness of approximately 170 nm. To ensure efficient charge transport between the anodic and cathodic electrochromic layers, a thin ITO conductive interlayer was subsequently deposited onto the NiO film by magnetron sputtering. $W_{18}O_{49}$ nanowires synthesized via a solvothermal route were then coated onto the ITO/NiO substrate as the cathodic electrochromic layer, enabling broadband modulation spanning the visible and near-infrared regions [28]. The elemental composition, phase, and morphology of $W_{18}O_{49}$ nanowires were confirmed by XPS (Fig. S1(b) in the ESM), XRD (Fig. S2 in the ESM), and TEM (Fig. S3(b) in the ESM), which are consistent with the previous report [29]. As shown in Figs. 1(e) and 1(f), the coated $W_{18}O_{49}$ nanowires form an entangled and porous network on top of the ITO/NiO layer, constituting an open composite electrode architecture. Such a structure facilitates electrolyte penetration and shortens ion diffusion pathways, while the embedded ITO interlayer provides a continuous electron-transport channel between the anodic and cathodic electrochromic components. The atomic composition depth profile of the multilayer structure of the composite electrode analyzed by XPS was further performed to confirm the tandem structure of the NIW electrode. To determine the atomic concentrations of the elements, depth profiling of the NIW composite electrode was performed using an ion beam, as shown in Fig. S4 in the ESM. With increasing etching time, the concentration of W gradually decreases, and the concentration of Ni steadily increases while the concentration of indium (In) first increases then decreases, reflecting the typical tandem structure of NIW with $W_{18}O_{49}$ in the upper layer, ITO in the middle layer, and NiO in the bottom layer.

3.2 Electrochromic properties of NIW electrode

The color change of $W_{18}O_{49}$ and NiO in 0.5 M $LiClO_4$/PC electrolyte solution is considered to be the reversible insertion/extraction of Li^+ at different potentials [30]. The coloration mechanism of $W_{18}O_{49}$ mainly involves the dual injection of electrolyte ions and electrons, which can induce bandgap transitions, phase transitions, and local surface plasmon resonance (LSPR, capacitance mechanism), resulting in modulation of visible and near-infrared light [21, 31]. It can be expressed by Eq. (1)

$$W_{18}O_{49}\ (\text{bleached}) + xLi^+ + xe^- \rightarrow Li_xW_{18}O_{49}\ (\text{colored}) \quad (1)$$

The electrochromic mechanism of NiO is divided into two steps, expressed by Eqs. (2) and (3) [32]. The first step involves the initial irreversible bleaching of deposited NiO. Once the Li_yNiO_x is formed, the reversible reaction between bleached Li_yNiO_x and colored $Li_{y-z}NiO_x$ can be realized to modulate the visible light, which can be observed as a color change from brown to transparent.

$$NiO_x + yLi^+ + ye^- \rightarrow Li_yNiO_x \quad (2)$$

$$Li_yNiO_x(\text{bleached}) \leftrightarrow Li_{y-z}NiO_x(\text{colored}) + zLi^+ + ze^- \quad (3)$$

The rationally designed porous architecture of the NIW electrode enables electrolyte ions to effectively access both the inner anodic NiO layer and the outer cathodic $W_{18}O_{49}$ layer, thereby allowing their electrochromic coloration processes to proceed independently under positive and negative biases, respectively (Fig. 2(a)). The high-resolution XPS spectra of Ni 2p and W 4f (Fig. S5 in the ESM) show that the Ni element in the NiO film predominantly exists as Ni^{2+} and Ni^{3+}, while the W element in the $W_{18}O_{49}$ film mainly exists as W^{5+} and W^{6+}. This corresponds to the electrochromic mechanism of the NIW electrode, wherein the insertion and removal of lithium ions alter the valence state of the electrochromic materials [33, 34]. Figures 2(b) and 2(c) show the transmission spectra and optical modulation of the NIW electrode spray-coated with 1.5 mL $W_{18}O_{49}$ dispersion solution under colored and bleached conditions at different electric potentials (0, 1.5, −1, and −1.5 V vs. Ag/AgCl). When under a bias of 0 V, the NIW electrode shows the bleached state with VIS transmittance of 81.5% and NIR transmittance of 69.6%, in which the lower NIR transmittance is caused by the blocking effect of the ITO substrate. Taking the spectrum at 0 V as the baseline, the NiO film in the NIW electrode becomes colored at 1.5 V, blocking 26.6% of solar radiation with 40.33% of VIS and 20.84% of NIR. At −1 V, the $W_{18}O_{49}$ nanowires in the NIW film become colored and block 62.48% of the solar radiation with 41.65% of the VIS and 83.54% of NIR. While at −1.5 V, $W_{18}O_{49}$ nanowires show a much darker color and further block 75.6% of the solar spectrum with 62.07% of VIS and 89.3% of NIR, which is particularly beneficial for reducing cooling energy demand under hot conditions.

To better illustrate the role of the conductive layer, the NW electrode was also prepared as a contrast. The typical electrochromic properties of NW electrodes with varying $W_{18}O_{49}$ contents are shown in Fig. S6 in the ESM, which include the transmission spectra (Fig. S6(a) in the ESM) and real-time transmittance change (Figs. S6(b) and S6(c) in the ESM). This indicates that NW electrodes can also perform the NiO and $W_{18}O_{49}$ electrochromic process separately under different potentials. The application of the same quantity of electrochromic material to the electrodes yielded no discernible variation in light transmittance modulation between the NW and NIW electrodes, while the NW electrode failed to return to the initial transmission state when the volume of $W_{18}O_{49}$ dispersion solution increased from 0.5 to 2 mL (Fig. S6(b) in the ESM). This limitation is effectively suppressed in the NIW electrode, highlighting the critical role of the conductive ITO interlayer [35]. As shown in Fig. S7 in the ESM, the real-time transmittance change of NIW electrodes with different sputtered ITO thicknesses was recorded, and it was found that the presence of the ITO layer can provide faster response time for the coloring/bleaching of $W_{18}O_{49}$ nanowire film from 9.65/4.4 to 8.61/3.43 s. In consideration of the cost performance, the conductive layer with a thickness of 100 nm was chosen for subsequent study. Figures 2(d) and 2(e) display the typical on/off electrochromic cycles of the NW and NIW electrodes with 1.5 mL $W_{18}O_{49}$ dispersion solution at 630 nm. The coloring time (t_c) of $W_{18}O_{49}$ decreased by 14.5%, and the bleaching time (t_b) was reduced by 53.4% from 10.1/7.06 to 8.64/3.29 s. NiO exhibited a 49.1% reduction in coloring time and a 37.6% reduction in bleaching time from 5.21/3.67 to 2.65/2.29 s. Similar improvements are also observed at 1000 nm (Fig. S8 in the ESM), with 20% (t_c) and 28.5% (t_b) improvement from 8.0/11.05 to 6.39/7.9 s. The response times of NW and NIW electrodes with different $W_{18}O_{49}$ contents at 630 and 1000 nm are detailed in Tables S1 and S2 in the

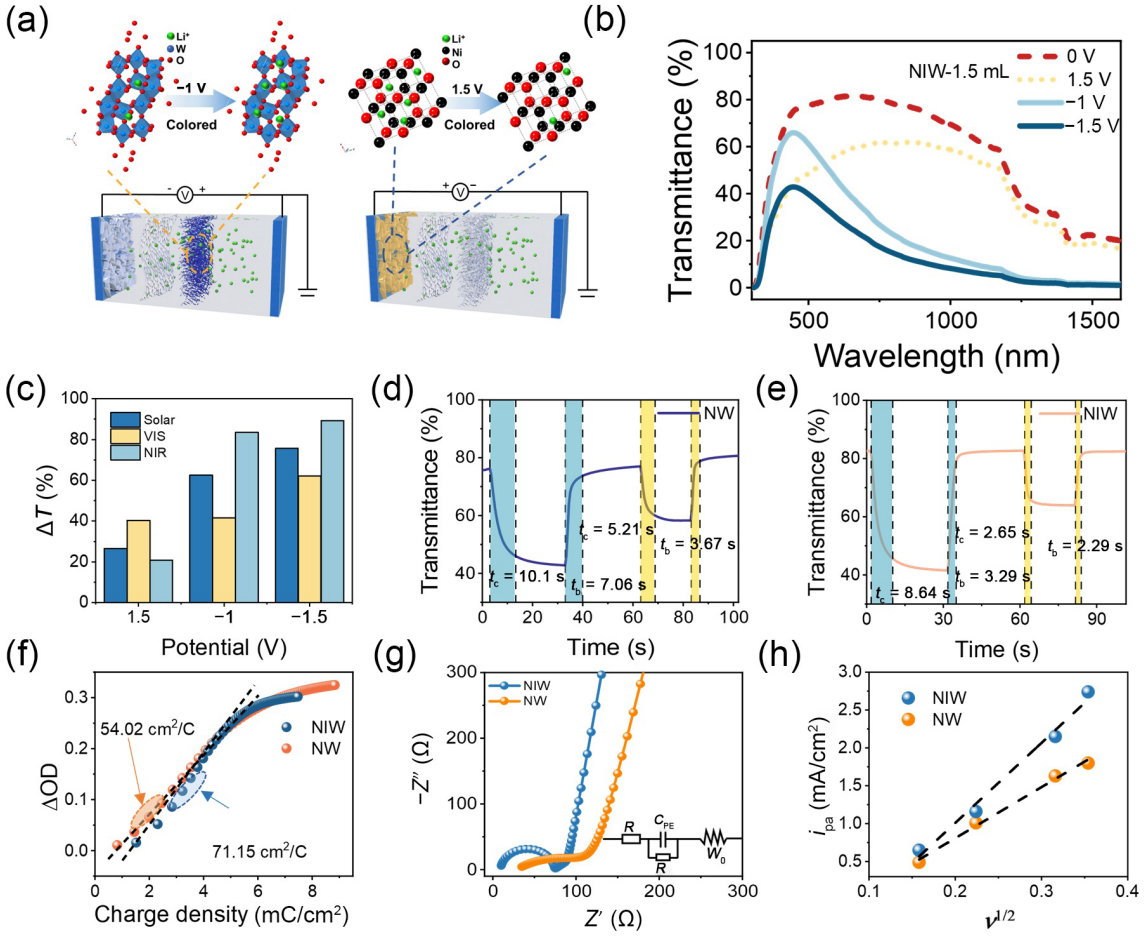

Figure 2 Characterization of optical and electrical properties of NW and NIW electrodes. (a) Electrochromic process of NIW electrode. (b) The transmission spectra of NIW film electrodes at different potentials (vs. Ag/AgCl). (c) Spectral modulation (ΔT) of NIW electrode at different potentials in the VIS, NIR, and whole solar spectrum regions, calculated after subtracting the baseline spectrum at 0 V. (d) and (e) Real-time transmittance change of NW and NIW electrodes monitored at 630 nm under −1, 0, 1.5, and 0 V (vs. Ag/AgCl) with 30 s interval, respectively. (f) Optical density (at 630 nm) versus charge density curves of NW and NIW electrodes. (g) The Nyquist plots for NW and NIW electrodes with an equivalent circuit. (h) Plots of cathode peak current densities versus the square root of scan rates for NW and NIW electrodes.

ESM. These enhancements originate from the ITO interlayer, which provides an efficient electron-transport pathway and facilitates coupled ion-electron transfer across the tandem electrochromic layers. The coloration efficiency of the NIW electrode with 1.5 mL $W_{18}O_{49}$ dispersion solution at 630 nm increases to 71.15 cm²/C (Fig. 2(f)), which is 24.1% higher than that of the NW electrode. The improvement in electrochromic performance of the NIW electrode can be attributed to the conductive ITO layer as the electron transfer medium, facilitating beneficial interactions with electrons and $W_{18}O_{49}$ nanowires for redox reactions [36–38].

To intrinsically connect these macroscopic speed improvements with microscopic reaction kinetics, we performed impedance measurements and cyclic voltammetry (CV), which further support the rapid diffusion of Li^+ within the NIW electrode. The intercalation mechanism of Li^+ on the surface of the NIW electrode in the electrolyte is well explained in the Nyquist diagram (Fig. 2(g)), and equivalent circuits are analyzed using Z-view software in the frequency range of 10^{-1} to 10^6 Hz. The solution resistor (R_s), charge transfer resistor (R_{ct}), double-layer capacitor (C_{dl}), and Warburg impedance (W) were calculated according to the fitting curve [38]. Compared with the NW electrode, the NIW electrode exhibits a markedly reduced R_{ct} of 64.16 Ω, in contrast to 102.3 Ω for the NW electrode, indicating significantly enhanced electronic conductivity. Meanwhile, the lower Warburg impedance of the NIW electrode (46.32 Ω) reflects faster Li^+ diffusion and reduced ion-transport resistance. CV curves of the NW and NIW electrodes recorded in the potential range from −1.5 to 1.5 V (Fig. S9 in the ESM) display well-defined redox peaks associated with $W_{18}O_{49}$ and NiO, consistent with their electrochromic behavior [39, 40]. Owing to the introduction of the conductive ITO interlayer, the peak current density of $W_{18}O_{49}$ increases markedly from 0.65 to 2.74 mA/cm², suggesting more efficient charge-transfer kinetics. To quantitatively evaluate Li^+ diffusion, CV measurements are further conducted at different scan rates (Fig. S10 in the EMS). As shown in Fig. 2(h), with increasing scan rate, the cathode peak shifts towards a higher positive potential, and the peak current density increases, indicating the ion diffusion-controlled electrochromic process [41]. For reactions related to ion diffusion behavior, the relationship between peak current and scan rate can be determined by Eq. (4)

$$i_p = 2.72 \times 10^5 n^{3/2} C_0 D^{1/2} \nu^{1/2} \quad (4)$$

where D is the diffusion coefficient, i_p is the peak current density, n is the number of electrons, C_0 is the concentration of active ions in the electrolyte, and ν is the scan rate. As shown in Fig. 2(h), the i_p of

the NW and NIW films has a good linear relationship with $v^{1/2}$, indicating that the insertion and extraction of ions are the diffusion-controlled processes [42].

In this study, for the NIW electrode with an active area (A) of 2.0 cm^2 and C_0 = 0.5 mol/L, the diffusion coefficient of Li^+ is calculated to be 6.04 × 10^{-9} cm^2/s. The diffusion coefficient of Li^+ ions in the NW electrode is calculated to be 2.46 × 10^{-9} cm^2/s. This enhancement further confirms that the NIW architecture effectively promotes Li^+ transport compared with both the NW electrode and previously reported electrochromic systems [43, 44].

3.3 The performance enhancement mechanism of the conductive layer in tandem structure

Figure 3(a) shows that the sputtered conductive layer introduces additional electron-transport pathways within the NIW electrode, allowing electrons to be transferred not only between the substrate and the NiO nanosheets, but also between the NiO nanosheets and $W_{18}O_{49}$ nanowires. This interfacial architecture is intrinsically supported by the cross-sectional energy-dispersive X-ray spectroscopy (EDS) mapping (Fig. S11 in the ESM). The elemental profiles of In and W clearly reveal that both the sputtered ITO and sprayed $W_{18}O_{49}$ are predominantly enriched at the top surface to form a continuous upper conductive network, while the ITO exhibits a penetrating gradient into the pores and macro-cracks of the underlying NiO layer. Consequently, electrons can be efficiently transferred not only from the substrate through the localized ITO penetrations, but also rapidly distributed across the top continuous ITO network into the $W_{18}O_{49}$ nanowires. The direction of charge transfer is determined by the difference in work function (Φ) or Fermi energy level (E_f) of the semiconductor heterojunction. As shown in Fig. 3(b), the work function of the ITO/NiO film is calculated to be 2.31 eV, which is lower than that of the NiO film (3.39 eV). Such a reduced Φ facilitates electron injection and transport, suppresses charge accumulation at the interface, and thereby enhances the electrochromic response of the NiO layer. The C-AFM test is further performed on the NiO electrode with a partially sputtered conductive layer. Figures 3(c) and 3(d) show the corresponding surface topography and current mapping, where the yellow-framed region represents areas covered by the conductive layer, while the blue-framed region corresponds to uncovered NiO. When the potential was applied to the tip of the C-AFM, the area containing the conductive layer showed a much larger current value (120–220 pA) compared to the area without the conductive layer (20–120 pA). More detailed characterization of regions with and without a conductive layer, as shown in Fig. S12 in the ESM, further confirms that the conductive layer simultaneously preserves the porous morphology of the NiO film while markedly enhancing local electrical conductivity. Furthermore, to exclude the interference of minor substrate flattening induced by ITO sputtering, the top-surface morphologies of the assembled NIW and NW electrodes were compared (Fig. S13 in the ESM). Both SEM and AFM analyses reveal that the macroscopic distribution and porous network of the spray-coated $W_{18}O_{49}$ nanowires remain highly consistent across both electrodes. Although the intermediate ITO layer slightly reduces the final surface roughness, this overall morphological consistency confirms that the enhanced electrochromic kinetics are intrinsically driven by the electrical optimization of the ITO interlayer, rather than structural advantages.

To further elucidate the role of the conductive interlayer in the NIW electrode, a simplified two-dimensional COMSOL Multiphysics model was constructed to simulate the evolution of Li^+ concentration during the lithiation process, as shown in Fig. 3(e). The sample size was set to 600 nm × 800 nm, and the boundary condition of the operating potential was 1.5 V. The simulated electrode structure consisted of a $W_{18}O_{49}$ nanowire layer, a porous conductive interlayer, and a NiO nanosheet layer arranged sequentially from top to bottom. A reference structure without the conductive interlayer was constructed for comparison. The simulation results demonstrate that, at the half-cell scale, the introduction of the conductive interlayer markedly accelerates Li^+ diffusion within the NIW electrode region.

Initially, the Li^+ concentration was zero in both the NW and NIW electrodes. After 40 s, the average concentration in the NIW electrode reached 0.21 mol/m^3, notably higher than that in the NW electrode (0.16 mol/m^3). By the 80-s mark, the NIW electrode had

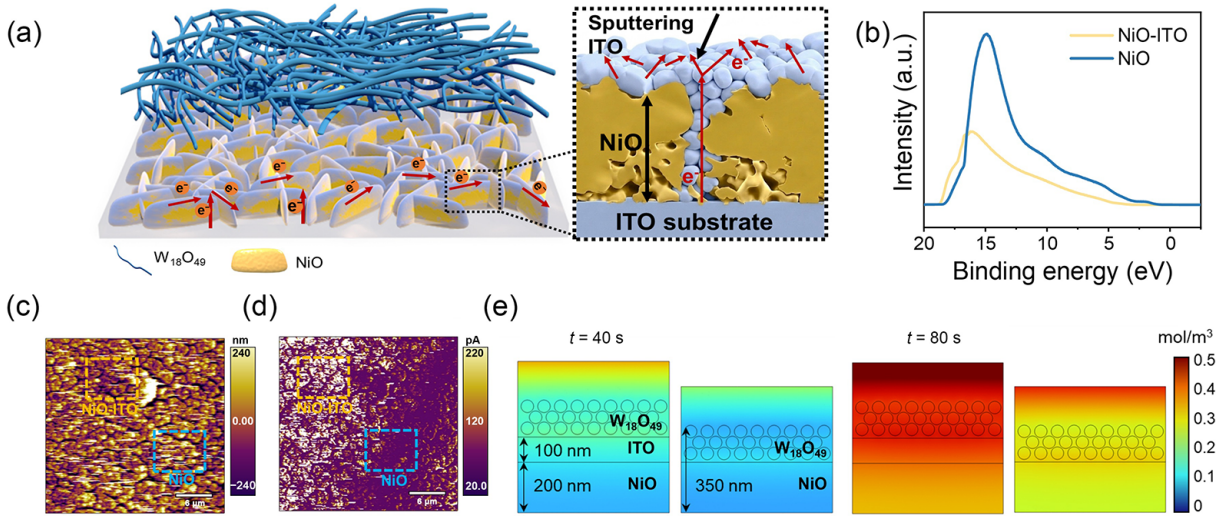

Figure 3 Mechanism of the conductive layer in the tandem structure. (a) Schematic diagram of the tandem structure of the NIW electrode and its conduction path. (b) The UPS spectra of the NiO and NiO-ITO thin film. (c) AFM image for NiO electrode with conductive layer (yellow frame) and without conductive layer (blue frame). (d) C-AFM image for NiO electrode with conductive layer (yellow frame) and without conductive layer (blue frame). (e) COMSOL simulation of Li^+ concentration gradient on NIW and NW electrodes.

attained a saturation level of 0.42 mol/m^3, while the NW electrode remained at 0.33 mol/m^3. This improvement can be ascribed to the porous conductive layer, which not only reduces electron transport resistance but also mitigates interfacial potential barriers, thereby promoting synergistic electron-ion transport and enhancing overall ionic mobility throughout the electrode.

3.4 Optical and electrical performance of NIW electrodes

Figures 4(a) and 4(b) illustrate the bias-dependent optical states of the NIW electrodes. At 0 V, the electrode is transparent, representing a bright mode. When a bias of −1 V is applied, the blue coloration of the electrodes becomes progressively deeper as the volume of the $W_{18}O_{49}$ dispersion increases from 0.5 to 2.0 mL, corresponding to the cool and dark modes. When the applied potential of the electrode was 1.5 V, the film only shows a lower transmittance of visible light, corresponding to the warm mode. The corresponding optical modulation is quantitatively summarized in Fig. 4(c). As the volume of $W_{18}O_{49}$ dispersion increases from 0.5 to 2.0 mL, the transmittance modulation (ΔT) of the NIW electrodes under −1 V increases from 18.49% to 44.53% at 630 nm and from 7.19% to 61.56% at 1000 nm (Fig. S14 in the ESM), demonstrating the effective amplification of VIS and NIR electrochromic responses through controlled loading of $W_{18}O_{49}$ nanowires. To further evaluate the dark-state performance, the $W_{18}O_{49}$ dispersion volume was increased up to 4 mL (Fig. S15 in the ESM), which achieved an impressive NIR optical modulation of 96.68%. However, an excessively thick film inevitably leads to a substantial increase in charge-transfer resistance, counteracting the kinetic advantages provided by the conductive ITO interlayer. Therefore, considering the trade-off between optical contrast and electrochemical kinetics, the 1.5 mL loading was selected as the optimal parameter for the device. The Nyquist diagrams of NIW and NW electrodes with different volumes of $W_{18}O_{49}$ dispersion solution are shown in Fig. 4(e) and Fig. S16 in the ESM. As the volume of $W_{18}O_{49}$ dispersion solution increases, the R_{ct}/Warburg impedance value of the NW electrode increases from 40.38/2195 to 217.9/7121 Ω, while R_{ct} values of NIW electrodes are in the range of 54.59–67.45 Ω, and the Warburg impedance value ranges from 46.32–80.84 Ω. This behaviour highlights the critical role of the ITO interlayer in mitigating electronic and ionic transport resistance within the tandem electrode architecture. The more detailed values of each parameter obtained by fitting the electrochemical impedance spectroscopy (EIS) curves of NW and NIW electrodes are summarized in Tables S3 and S4 in the ESM, and the corresponding bar chart for R_{ct} is shown in Fig. S17 in the ESM. Cycling stability is further evaluated to assess the long-term electrochromic performance of the NIW electrode. The NIW electrode demonstrates long-term durability, maintaining a capacity retention of 90.1% after 1000 cycles, and even after an extended testing period of 2000 cycles, it still exhibits a robust retention rate of 85.1% (Fig. 4(f) and Fig. S18 in the ESM). For comparison, the NW electrode (without the ITO layer) was tested under the same conditions, and its retention rate dropped to 87.7% after 1000 cycles. The more severe degradation behaviour of the NW electrode is primarily attributed to the interfacial issues. Repeated ion insertion/extraction inevitably generates complex interfacial residual stresses. For the NW electrode, the absence of the ITO intermediate layer leads to poor interfacial contact between the bottom NiO and the top $W_{18}O_{49}$. Under continuous interfacial stress during cycling, the physical adhesion weakens, causing the interfacial charge transfer resistance to significantly increase over time. In contrast, the magnetron-sputtered ITO layer in the NIW electrode acts as an effective buffer layer and a strong conductive binder, which helps maintain good mechanical and electrochemical integrity over long-term operation. The detailed transmittance

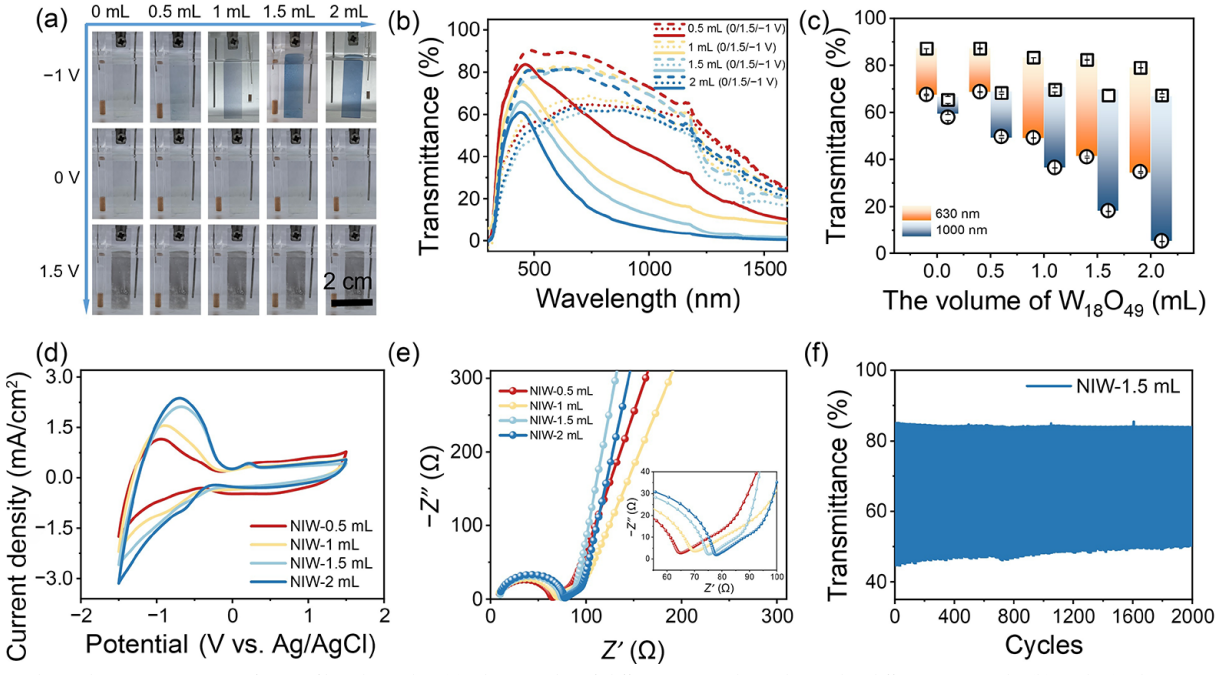

Figure 4 Electrochromic properties of NIW film electrodes. (a) Photographs of different NIW electrodes under different potentials. (b) and (c) The UV–VIS–NIR transmission spectra and modulation rates at 630/1000 nm of NIW electrodes with different $W_{18}O_{49}$ contents at −1, 0, and 1.5 V. (d) and (e) The cyclic voltammetry curves and Nyquist plots of NIW electrodes with different $W_{18}O_{49}$ nanowire contents. (f) Continuous recording of the NIW electrode transmittance spectrum monitored at 630 nm for 2000 switching cycles, with each cycle operated at −1 V (the coloration voltage for $W_{18}O_{49}$), 0 V (the bleaching voltage), 1.5 V (the coloration voltage for NiO), and 0 V (the bleaching voltage) for 30 s, respectively.

switching curves are shown in Fig. S19 in the ESM. The slight ΔT loss of the NIW electrode during the cycle may be caused by the irreversible capture of Li^+ at $W_{18}O_{49}$ and NiO regions [45, 46].

3.5 Application of multimode electrochromic devices with tandem structure

The multimode electrochromic device with a size of 4 cm × 4 cm was prepared by using a simple layer-by-layer assembly method with the NiO/ITO counter electrode. The solar irradiance transmittance in different states was calculated to quantify the practical solar irradiance modulation performance, as shown in Fig. 5(a). The ΔT of the multimode electrochromic device under 0 V (Fig. S20 in the ESM) is presented in Fig. 5(b). At 2.5 V, the NiO layer in the device undergoes a color change, resulting in an 18.86% solar spectrum modulation with a VIS difference of 29.96% and an 8.73% difference in NIR. At −2 V, the $W_{18}O_{49}$ layer becomes colored, enhancing the device to block 72.44% of solar radiation, with 42.26% of VIS and 71.13% of NIR. When the bias increases to −2.5 V, the device further modulates the solar spectrum by 88.43% with 74.96% of VIS and 98.35% of NIR. This broadband and multimode spectrum modulation capability allows the device to dynamically alter its optical appearance while maintaining passive environmental adaptability, making it suitable for applications such as privacy protection and anti-counterfeiting. As a proof of concept, an electrochromic device with a butterfly pattern was fabricated and operated in several modes, as depicted in Fig. 5(c). When a positive potential (2.5 V) was applied to both sides of the device, it appeared brown. While a negative potential (−2.5 V) was applied to the left side and a positive potential (2.5 V) was applied to the right, the device displayed different colors on each side simultaneously, demonstrating spatially independent and addressable electrochromic modulation. Furthermore, the thermal regulation performance of the multistage smart window was systematically evaluated. The smart window with an area of 4 cm × 4 cm was installed on a model chamber with a black cylinder placed at the center as an absorber.

The model room was exposed to simulated solar light (the illumination intensity is 100 mW/cm^2), aligning the blackbody, window, and light source. Infrared cameras and thermocouples were used to record the blackbody and air temperatures at the center of the model room in real-time, thereby assessing the cooling performance of the smart window (Figs. 5(d) and 5(e)). After 20 min of direct irradiation, the blackbody temperature of the room with the blank glass was 53.4 °C. In contrast, when the multistage smart window was operated at biases of 2.5, −2.0, and −2.5 V, the absorber temperatures were stabilized at 42.3, 36.0, and 32.2 °C, respectively. The corresponding infrared images are shown in Fig. S21 in the ESM. These results demonstrate that the multistage smart window can reduce the blackbody temperature in the model chamber by up to 21.2 °C and the air temperature by 3.39 °C compared to the blank glass, as shown in Fig.5(f). In addition, the NIW device was subjected to 500 continuous charge/discharge cycles. The device can maintain 87.14% of its initial optical modulation after 400 continuous charge/discharge cycles. However, the transmittance modulation quickly dropped to 62.86% during the 400–500 cycles. This degradation can be attributed to the device-level limitation related to the electrolyte and the encapsulation of the device. Furthermore, the energy required to operate the device is extremely low, with a calculated energy consumption of approximately 5.8 Wh/m^2. This minute electrical energy requirement underscores its potential as a highly efficient energy-saving component for modern green buildings.

4 Conclusions

In summary, a tandem-structured electrochromic electrode integrating anodic and cathodic electrochromic materials on a single substrate was successfully constructed, enabling multicolor and dual-band spectral modulation. Under applied potentials of 1.5, 0, and −1 V (vs. Ag/AgCl), the electrode exhibits reversible color

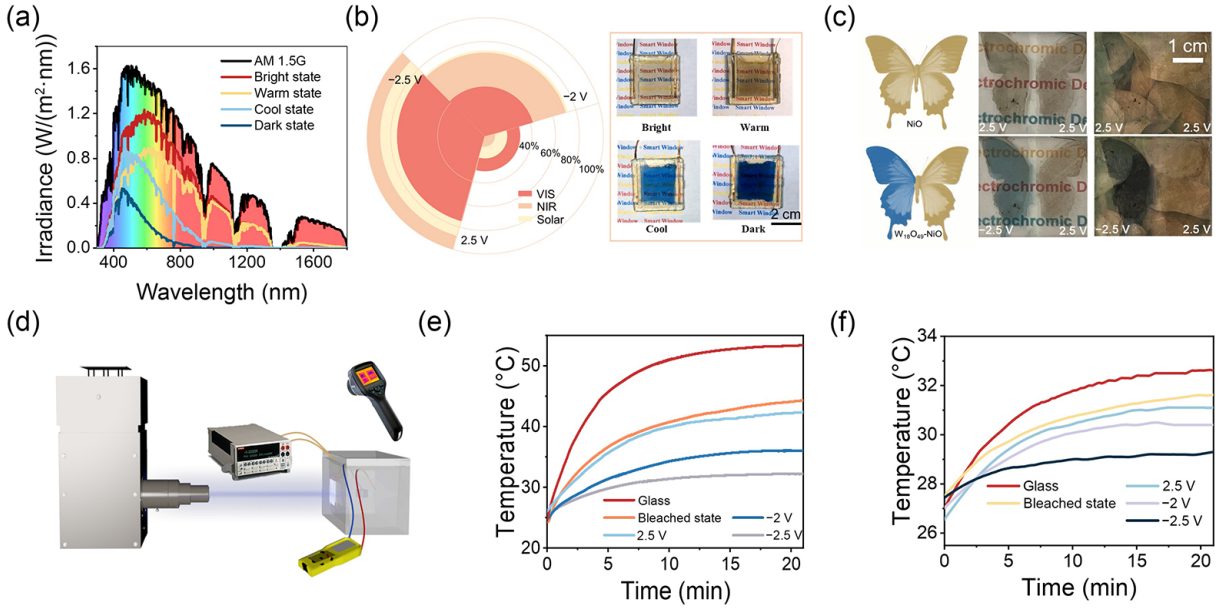

Figure 5 Multimode electrochromic device for smart window and anti-counterfeiting applications. (a) Solar irradiance spectra of the multimode electrochromic device in different states. (b) The ΔT of the multimode electrochromic device under different biases in the VIS, NIR, and whole solar spectral regions (calculated after subtracting the baseline spectrum at 0 V), along with corresponding photographic images. (c) The digital photos of the tandem structure electrode with different parts under different potentials for anti-counterfeiting and privacy protection functions. (d) Schematic illustration for the indoor cooling performance study of the multimode electrochromic device. (e) and (f) The temperature change of the blackbody and air under the light irradiation in a model room for 20 min with the smart window under different potentials.

transitions from brown to transparent and then to blue. The introduction of a conductive interlayer between the composite electrochromic layers (NiO and $W_{18}O_{49}$) markedly enhances electron transport and ion diffusion, resulting in improved response kinetics and coloration efficiency. The effects of the nanocomposite architecture on the optical and electrochemical properties were systematically elucidated. Based on this design, a multiband-regulated electrochromic device was further demonstrated, offering adaptable functionality across diverse application scenarios. This structure can serve as a common template for dual-function electrochromic devices and holds substantial potential in the field of energy-saving smart windows and multicolor displays.

Electronic Supplementary Material: Supplementary material (including additional characterization results, SEM images, TEM images, XRD spectra, UV–VIS spectra, time response curves, Nyquist plots, and infrared images) is available in the online version of this article at https://doi.org/10.26599/NR.2026.94908696.

Data availability

All data needed to support the conclusions in the paper are presented in the manuscript and the Electronic Supplementary Material. Additional data related to this paper may be requested from the corresponding author upon request.

Acknowledgements

This work was financially supported by the National Natural Science Foundation of China (No. 52373243, 22575112, 52503317, and 224B2504), Shenzhen Science and Technology Program (No. JCYJ20220530113200002, KQTD20221101093559017, and ZDSYS20220401161800001), Guangdong Provincial Key Laboratory of Sustainable Biomimetic Materials and Green Energy (No. 2024B1212010003), Guangdong Innovative and Entrepreneurial Research Team Program (No. 2023ZT10C027), High level of special funds (No. G03050K002), and the New Cornerstone Science Foundation.

Declaration of competing interest

All the contributing authors reports no conflict of interests in this work. Author Shu-Hong Yu is the advisory board member of this journal, but he is not involved in the peer-review or decision of this article.

Author contribution statement

M.-H. Z., J.-L. W., and S.-H. Y. conceived the idea and designed the experiments. J.-L. W. and S.-H. Y. supervised the research. M.-H. Z., S.-Z. S., and J.-L. W. carried out the synthesis experiment and analysis. F.-X. Z. and C. C. helped with the COMSOL simulation. M.-H. Z., C. C., X.-F. H. and S.-Z. S. helped with the UV-VIS-NIR spectra. Z.-Y. H. and C. C. assisted with the TEM and SEM testing. X.-F. H. helped with the AFM and CAFM testing. S.-H. Y., M.-H. Z., J.-L. W., and S.-Z. S. analyzed the data and co-wrote the manuscript. All authors analyzed and discussed the results.

Use of AI statement

None.

References

[1] Chen, D. H.; Tong, Z. Z.; Rao, Q. S.; Liu, X. C.; Meng, H.; Huang, W. High-performance black copolymers enabling full spectrum control in electrochromic devices. *Nat. Commun.* **2024**, *15*, 8457.
[2] Wang, J.; Li, Z. H.; Liu, X. Y.; Su, B. C.; Gong, H. H.; Feng, C.; Li, G. P.; He, G.; Rao, B. Fine-tuning redox ability of arylene-bridged bis(benzimidazolium) for electrochromism and visible-light photocatalysis. *Chin. Chem. Lett.* **2024**, *35*, 109473.
[3] Chen, Y. Y.; Wang, Z.; Fan, B. W.; Zhang, C. Y.; Li, S. L.; Tang, X. Q.; Li, Y. W.; Wang, X. Y.; Wang, C. H.; Li, D. et al. Temperature-tolerant electrochromic devices enabled by LiCl water-in-salt electrolyte with excellent performance. *Chin. Chem. Lett.* **2026**, *37*, 110824.
[4] Sui, C.; Pu, J. K.; Chen, T. H.; Liang, J. W.; Lai, Y. T.; Rao, Y. F.; Wu, R. H.; Han, Y.; Wang, K. Y.; Li, X. Q. et al. Dynamic electrochromism for all-season radiative thermoregulation. *Nat. Sustain.* **2023**, *6*, 428–437.
[5] Tang, X. Q.; Hu, Z. S.; Wang, Z.; Wang, Z. Y.; Li, Y. W.; Cong, S.; Zhao, Z. G. A multicolor electrochromic device with on-demand solar thermal management for smart building envelopes. *Nano Res.* **2025**, *18*, 94907005.
[6] Deb, S. K. A novel electrophotographic system. *Appl. Opt.* **1969**, *8*, 192–195.
[7] Tang, X. Q.; Hu, Z. S.; Wang, Z. Y.; Wu, X. Z.; Wang, Z.; Su, W. M.; Cong, S.; Geng, F. X.; Zhao, Z. G. Super-wide color tunability from a single electrochromic device through *in situ* reconstruction of optical cavity. *Adv. Mater.* **2025**, *37*, 2417511.
[8] Zhang, T. Y.; Mu, X. Y.; Li, Y. W.; Cong, S.; Zheng, S. N.; Huang, R.; Geng, F. X.; Zhao, Z. G. Optical-cavity-incorporated colorful all-solid-state electrochromic devices for dual anti-counterfeiting. *Adv. Mater.* **2024**, *36*, 2402670.
[9] Chen, Y. N.; Lei, J.; Zhai, Y. L.; Zhu, Z. J.; Wu, W. T.; Lu, X. Q. Tungsten oxide nanowires and polyaniline hybrid film-based electrochromic device with multicolor display and enhanced capacitance. *Chin. Chem. Lett.* **2023**, *34*, 108305.
[10] Wang, J. L.; Liu, J. W.; Sheng, S. Z.; He, Z.; Gao, J.; Yu, S. H. Manipulating nanowire assemblies toward multicolor transparent electrochromic device. *Nano Lett.* **2021**, *21*, 9203–9209.
[11] Jia, Z. F.; Sui, Y.; Qian, L.; Ren, X.; Zhao, Y. X.; Yao, R.; Wang, L. M.; Chao, D. L.; Yang, C. Electrochromic windows with fast response and wide dynamic range for visible-light modulation without traditional electrodes. *Nat. Commun.* **2024**, *15*, 6110.
[12] Xiao, C.; Wang, C. C.; Zhang, L. P.; Fu, S. H. A multimode dynamic color-changing device for smart windows based on integrating thermochromic and electrochromic properties. *ACS Appl. Mater. Interfaces* **2024**, *16*, 60678–60685.
[13] Huang, Y.; Wu, S. D.; Zhao, S. M.; Guo, Z. Y.; Zhao, Z. J.; Wu, X. K.; Wang, B. S.; Wang, F.; Xi, A. K.; Lan, F. et al. A novel liquid flow electrochromic smart window for all-year-round dynamic photothermal regulation. *Energy Environ. Sci.* **2025**, *18*, 1824–1834.
[14] Navya, P. V.; Sampath, S. A first truly hydrocarbon-based electrochromic molecule exhibiting transparent-to-dark switching and heavy atom effect of bromine in color shifting. *Adv. Funct. Mater.* **2025**, *35*, 2411783.
[15] Shao, Z. W.; Huang, A. B.; Cao, C. C.; Ji, X. W.; Hu, W.; Luo, H. J.; Bell, J.; Jin, P.; Yang, R. G.; Cao, X. Tri-band electrochromic smart window for energy savings in buildings. *Nat. Sustain.* **2024**, *7*, 796–803.
[16] Zhou, Y. P.; Lv, Y.; Guo, X. D.; Wang, X. Y.; Liu, Z. Q.; Wang, J.; Sui, Q.; Wang, J. H.; Zeng, Z. Y.; Cai, G. F. Electrochromic smart windows with on-demand photothermal regulation for energy-saving buildings. *Adv. Mater.* **2025**, *37*, 2502706.
[17] Ma, Y.; Wang, Y. B.; Zhou, J. Y.; Lan, Y. Y.; Jiang, S.; Ge, Y. F.; Tan, S.; Zhang, S. G.; Wang, C. H.; Wu, Y. LCST ion gels fabricating "all-in-one" smart windows: Thermotropic, electrochromic and power-generating. *Mater. Horiz.* **2024**, *11*, 3825–3834.

[18] Wu, W. T.; Poh, W. C.; Lv, J.; Chen, S. H.; Gao, D. C.; Yu, F.; Wang, H.; Fang, H. J.; Wang, H.; Lee, P. S. Self-powered and light-adaptable stretchable electrochromic display. *Adv. Energy Mater.* **2023**, *13*, 2204103.

[19] Wang, Z.; Wang, X. Y.; Cong, S.; Geng, F. X.; Zhao, Z. G. Fusing electrochromic technology with other advanced technologies: A new roadmap for future development. *Mater. Sci. Eng.: R: Rep.* **2020**, *140*, 100524.

[20] Thi Phan, G.; Van Pham, D.; Doan Thi, N. L.; Sta. Maria, C.C.; Chu, Y. H.; Ma, Y. R. Nanorod-based smart windows with solid-gel electrolyte: An integrated electrochromic and pseudocapacitive technology for energy-saving and conversion. *Nano Energy* **2024**, *132*, 110374.

[21] Hassan, M.; Ghaffar, A.; Lou, G.; Miao, Z. A.; Peng, Z. C.; Celebi, K. Enhanced transport kinetics of electrochromic devices by $W_{18}O_{49}$ NW/$Ti_3C_2T_x$ composite films. *Adv. Funct. Mater.* **2024**, *34*, 2310535.

[22] Nisa, M. U.; Nadeem, N.; Yaseen, M.; Iqbal, J.; Zahid, M.; Abbas, Q.; Mustafa, G.; Shahid, I. Applications of graphene-based tungsten oxide nanocomposites: A review. *J. Nanostruct. Chem.* **2023**, *13*, 167–196.

[23] Li, J. F.; Chen, X. J.; Zhu, X. J.; Jiang, Y. C.; Chang, X. T.; Sun, S. B. Two-dimensional transition metal mxene-based gas sensors: A review. *Chin. Chem. Lett.* **2024**, *35*, 108286.

[24] Zhao, Q.; Fang, Y. S.; Qiao, K.; Wei, W.; Yao, Y. J.; Gao, Y. Printing of WO_3/ITO nanocomposite electrochromic smart windows. *Sol. Energy Mater. Sol. Cells* **2019**, *194*, 95–102.

[25] Zhang, C. H.; Chen, X.; Zhou, Y. T.; Si, Y. P.; Wang, H. C.; Zhao, Q.; Guan, X.; Gao, Y. F. Silver nanowires/WO_3 quantum dots electrode with enhanced vertical electric field gradient for Al^{3+}/Li^+ dual-functional electrochromic supercapacitor. *Next Mater.* **2025**, *6*, 100280.

[26] Saadeddin, I.; Suleiman, M.; Salman, H.; Zrikem, K.; Song, G.; Rougier, A. Optimization of low value electrodeposition parameters of nano-structured nio electrochromic thin films. *Solid State Ionics* **2019**, *343*, 115129.

[27] Yuan, Y. F.; Xia, X. H.; Wu, J. B.; Chen, Y. B.; Yang, J. L.; Guo, S. Y. Enhanced electrochromic properties of ordered porous nickel oxide thin film prepared by self-assembled colloidal crystal template-assisted electrodeposition. *Electrochim. Acta* **2011**, *56*, 1208–1212.

[28] Wang, J. L.; Lu, Y. R.; Li, H. H.; Liu, J. W.; Yu, S. H. Large area co-assembly of nanowires for flexible transparent smart windows. *J. Am. Chem. Soc.* **2017**, *139*, 9921–9926.

[29] Sun, X. H.; Wu, W.; Liu, N. N.; Li, P.; Zhao, X. Y.; Qu, Z. Z.; Zhao, K. M.; Wang, B.; Rong, X. H.; Zhang, X. Y. et al. Controlled assembly and synthesis of oxygen-deficient $W_{18}O_{49}$ films based on solvent molecular strategy for electrochromic energy storage smart windows. *Chem. Eng. J.* **2024**, *499*, 156109.

[30] Da Rocha, M.; He, Y. C.; Diao, X. G.; Rougier, A. Influence of cycling temperature on the electrochromic properties of WO_3//NiO devices built with various thicknesses. *Sol. Energy Mater. Sol. Cells* **2018**, *177*, 57–65.

[31] Li, K. R.; Shao, Y. L.; Yan, H. P.; Lu, Z.; Griffith, K. J.; Yan, J. H.; Wang, G.; Fan, H. W.; Lu, J. Y.; Huang, W. et al. Lattice-contraction triggered synchronous electrochromic actuator. *Nat. Commun.* **2018**, *9*, 4798.

[32] Wen, R. T.; Granqvist, C. G.; Niklasson, G. A. Anodic electrochromism for energy-efficient windows: Cation/anion-based surface processes and effects of crystal facets in nickel oxide thin films. *Adv. Funct. Mater.* **2015**, *25*, 3359–3370.

[33] Peck, M. A.; Langell, M. A. Comparison of nanoscaled and bulk NiO structural and environmental characteristics by XRD, XAFS, and XPS. *Chem. Mater.* **2012**, *24*, 4483–4490.

[34] Chang, Y. H.; Wang, Z. G.; Shi, Y. E.; Ma, X. C.; Ma, L.; Zhang, Y. Q.; Zhan, J. H. Hydrophobic $W_{18}O_{49}$ mesocrystal on hydrophilic PTFE membrane as an efficient solar steam generation device under one sun. *J. Mater. Chem. A* **2018**, *6*, 10939–10946.

[35] Yin, Y.; Lan, C. Y.; Guo, H. Y.; Li, C. Reactive sputter deposition of WO_3/Ag/WO_3 film for indium tin oxide (ITO)-free electrochromic devices. *ACS Appl. Mater. Interfaces* **2016**, *8*, 3861–3867.

[36] Dutta, P.; Goswami, S.; Roy, R.; Singh, A. K. Spray-coated $W_{18}O_{49}$/$Ti_3C_2T_x$ mxene electrodes for high-performance electrochromic energy storage devices. *Small* **2025**, *21*, 2503529.

[37] Zhang, S. L.; Li, Y.; Zhang, T. R.; Cao, S.; Yao, Q. F.; Lin, H. B.; Ye, H. L.; Fisher, A.; Lee, J. Y. Dual-band electrochromic devices with a transparent conductive capacitive charge-balancing anode. *ACS Appl. Mater. Interfaces* **2019**, *11*, 48062–48070.

[38] Goel, R.; Jha, R.; Ravikant, C. Synergistic effect of urea and potassium sulphate during hydrothermal synthesis of NiO nanospheres with reduced crystallite size and enhanced electrical conductivity. *Inorg. Chem. Commun.* **2022**, *141*, 109563.

[39] Pan, J. B.; Zheng, R. Z.; Wang, Y.; Ye, X. K.; Wan, Z. Q.; Jia, C. Y.; Weng, X. L.; Xie, J. L.; Deng, L. J. A high-performance electrochromic device assembled with hexagonal WO_3 and NiO/PB composite nanosheet electrodes towards energy storage smart window. *Sol. Energy Mater. Sol. Cells* **2020**, *207*, 110337.

[40] Phan, G. T.; Pham, D. V.; Patil, R. A.; Tsai, C. H.; Lai, C. C.; Yeh, W. C.; Liou, Y.; Ma, Y. R. Fast-switching electrochromic smart windows based on NiO-nanorods counter electrode. *Sol. Energy Mater. Sol. Cells* **2021**, *231*, 111306.

[41] Zhou, K. L.; Wang, H.; Zhang, S. J.; Jiu, J.; Liu, J. B.; Zhang, Y. Z.; Yan, H. Electrochromic modulation of near-infrared light by WO_3 films deposited on silver nanowire substrates. *J. Mater. Sci.* **2017**, *52*, 12783–12794.

[42] Huang, J. J.; Zhang, S. Y.; Qin, Q.; Wang, Z. P.; Cai, G. F. Designing V_2O_5/mxene van der waals heterostructure for complementary electrochromic dual-ion capacitor. *Chem. Eng. J.* **2023**, *476*, 146626.

[43] Liang, L.; Zhang, J. J.; Zhou, Y. Y.; Xie, J. F.; Zhang, X. D.; Guan, M. L.; Pan, B. C.; Xie, Y. High-performance flexible electrochromic device based on facile semiconductor-to-metal transition realized by $WO_3 \cdot 2H_2O$ ultrathin nanosheets. *Sci. Rep.* **2013**, *3*, 1936.

[44] Zhang, L. M.; Zeng, H.; Wu, J.; Pan, C. Z.; Zeng, F.; Gao, Y. F. Polyaniline/$WO_{2.86}$ composite film for dual-band electrochromic smart windows. *Sol. Energy Mater. Sol. Cells* **2025**, *286*, 113568.

[45] Tian, M. F.; Zheng, R. Z.; Jia, C. Y. Bridging to commercialization: Record-breaking of ultra-large and superior cyclic stability tungsten oxide electrochromic smart window. *Adv. Mater.* **2025**, *37*, 2409790.

[46] Zhang, R. F.; Zhou, Q. Q.; Huang, S. Y.; Zhang, Y. W.; Wen, R. T. Capturing ion trapping and detrapping dynamics in electrochromic thin films. *Nat. Commun.* **2024**, *15*, 2294.